Silicon (2018) 10:1687–1696
https://doi.org/10.1007/s12633-017-9653-7

ORIGINAL PAPER

The Impact of Ni Substitution on the Structural and Magnetic Properties of Mg Nano-Ferrite

Ebtesam E. Ateia[1] · Asmaa A. H. El-Bassuony[1] · Galila Abdellatif[1] · Amira T. Mohamed[1]

Received: 2 June 2016 / Accepted: 3 October 2017 / Published online: 10 January 2018

Abstract Magnesium substituted nickel nano-ferrite $Mg_{1-x}Ni_xFe_2O_4$ (x = 0.0, 0.1, 0.3, 0.5, 0.7, and 1.0) was synthesized by the citrate-gel auto-combustion method. Synthesized powders were sintered at 600 °C for 4 hours and characterized by X-ray, High Transmission Electron Microscopy, Brunauer-Emmett-Teller, Atomic Force Microscopy and Energy Dispersive X-ray Spectroscopy analyses. The impact of replacing Mg ions by Ni on the structural parameters and magnetic properties of the system was investigated utilizing X-ray diffraction and χ–T magnetic measurements at room and low temperatures. The crystallite sizes were found in the range of 24.6 nm – 27.6 nm. The variation of lattice parameter, the roughness, surface area and the porosity size upon increasing the Ni content were determined and then correlated with the cation distribution and the magnetic behavior. The coercivity (H_c) values vary from 56.4 Oe to 130 Oe. These values make the investigated samples well suited for their use in recording media. Magnetic parameters such as saturation magnetization, and Curie temperature (T_c) assured the existence of a critical concentration at x = 0.3 in which the anomalous character appeared.

Keywords Roughness · Surface area · Magnetic susceptibility · Magnetic moment

✉ Galila Abdellatif
galila@sci.cu.edu.eg

[1] Physics Department, Faculty of Science, Cairo University, Giza, Egypt

1 Introduction

Soft ferrites are most versatile in their technological applications [1–3]. Recently special focus has been placed on obtaining ferrite as a particulate environment through unusual methods, especially chemical methods [4]. Chemical methods provide uniform distribution of ions at the molecular level, high purity of the products and an efficiency of practically 100%.

Magnesium ferrite ($MgFe_2O_4$) is an important material in the category of cubic spinel ferrite. The spinel name is given due to its structure in which metal ions are distributed between tetrahedral (A site) and octahedral (B site) sites in a unit cell formed by oxygen ions [5–7]. The distribution of metal ions through the A site and B site affects the magnetic properties of $MgFe_2O_4$, which may be controlled by thermal treatment and crystallite size [8–10].

Magnesium ferrite belongs to the soft magnetic materials group, which is easily magnetized and demagnetized So it shows a good potential for novel applications as humidity control, drug delivery, data storage and transmission, spintronics, microwaves and sensors [11–14].

A lot of efforts have been carried out for the synthesis of Mg Fe_2O_4 with improved magnetic and physical properties [15].

The electrical, structural and magnetic properties of magnesium can be tailored either by changing the microstructure or by incorporation of different metal ions [16]. Several researchers have studied transition metal substituted magnesium ferrites to enhance their properties such as Mg-Co/Ca [17], Mg-Cu [18], and Mg- Zn [19].

In view of the immense importance of magnesium nano-ferrites, an initial attempt has been made to investigate the effect of Ni ions substitution on the structural and magnetic properties of Mg nano-ferrite. Among the different chemical methods, the citrate method was used to synthesize Mg-Ni

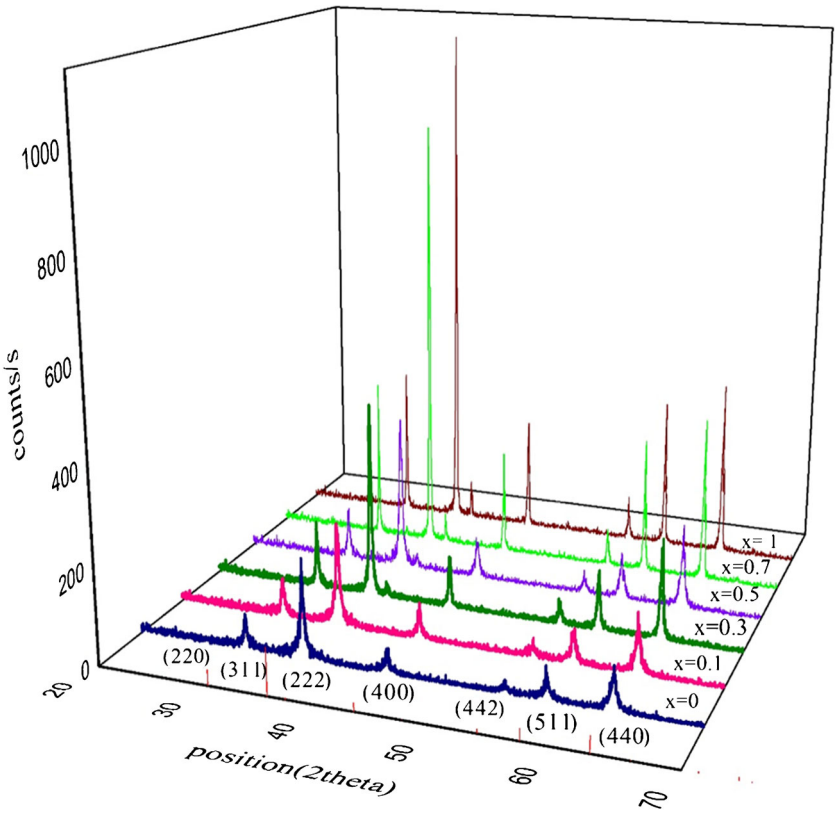

Fig. 1 X-ray diffraction patterns for $Mg_{1-x}Ni_xFe_2O_4(0.0 \leq x \leq 1.0)$

nano-ferrite, which yields renewable, high purity, ultrafine single-phase nano-crystalline ferrites, giving a homogeneous mixture of metal ions and a relatively low cost process as compared with other wet chemical synthesis processes.

2 Experimental Work

$Mg_{1-x}Ni_xFe_2O_4$ (x = 0.0, 0.1, 0.3, 0.5, 0.7, and 1.0) samples were synthesized using stoichiometric amounts of high purity (99.9%, Fisher chemicals) iron, magnesium, nickel nitrates, and citric acid using deionized water as a solvent. The structure and crystallite sizes were tested by X-ray diffraction (XRD) patterns using Diano Corporation target Cu-Kα (λ =1.5418 Å). The nanoparticles average sizes were estimated using Scherrer's relationship [20]. Morphological and microstructural characterization of the nano-ferrite samples were studied by high resolution transmission electron microscopy (HRTEM). Complimentary information about the surface microstructure of the investigated samples was obtained from the three dimensional atomic force microscopy (AFM) images using a WET-SPM-9600 scanning probe microscope. The specific surface area was determined by the Brunauer-Emmett-Teller (BET) method [21] based on adsorption/desorption isotherms of nitrogen at 77 K obtained with a NOVA 2200, USA, automated gas sorption system. The chemical composition of the investigated samples was measured to confirm the stoichiometric ratio of a given system using energy dispersive X-ray analyses (EDAX). The room temperature magnetic hysteresis loops of the investigated samples were measured using a vibrating sample magnetometer (VSM) model: Lake Shore 7410.

Table 1 Values of radii of tetrahedral and octahedral sites, experimental and theoretical lattice parameter, X-ray density, and microstrain for $Mg_{1-x}Ni_xFe_2O_4$ ($0.0 \leq x \leq 1.0$)

Ni content (X)	Cation distribution	r_A (Å)	r_B (Å)	a_{exp} (Å)	a_{th} (Å)	D_x(gm/cm^3)	Strain $\times 10^{-3}$
0.0	$(Mg^{2+}_{0.1}\ Fe^{3+}_{0.9})\ [Mg^{2+}_{0.9}Fe^{3+}_{1.1}]\ O_4$	0.498	0.679	8.397	8.381	8.381	4.300
0.1	$(Mg^{2+}_{0.09}Fe^{3+}_{0.91})[Ni^{2+}_{0.1}Mg^{2+}_{0.81}Fe^{3+}_{1.09}]\ O_4$	0.497	0.678	8.391	8.377	8.377	4.300
0.3	$(Mg^{2+}_{0.07}Fe^{3+}_{0.93})[Ni^{2+}_{0.3}Mg^{2+}_{0.63}Fe^{3+}_{1.07}]\ O_4$	0.496	0.675	8.382	8.369	8.369	4.600
0.5	$(Mg^{2+}_{0.05}\ Fe^{3+}_{0.95})\ [Ni^{2+}_{0.5}Mg^{2+}_{0.45}Fe^{3+}_{1.05}]\ O_4$	0.494	0.673	8.373	8.360	8.360	4.800
0.7	$(Mg^{2+}_{0.03}Fe^{3+}_{0.97})[Ni^{2+}_{0.7}Mg^{2+}_{0.27}Fe^{3+}_{1.03}]\ O_4$	0.492	0.671	8.354	8.352	8.352	3.200
1.0	$(Fe^{3+}_{1.0})\ [Ni^{2+}_{1.0}Fe^{3+}_{1.0}]\ O_4$	0.490	0.668	8.341	8.339	8.339	2.900

3 Results and Discussion

XRD patterns for nano-ferrite samples of the general formula $Mg_{1-x}Ni_xFe_2O_4$; (x=0.0, 0.1, 0.3, 0.5, 0.7 and 1) are shown in Fig. 1. The XRD patterns are compared and indexed using ICDD card no. (01-074-6653).The patterns show well-defined broad Bragg peaks and no impurity phase has been identified in any of the samples. The fundamental reflections from the crystal planes (220), (311), (222), (400), (422), (511) and (440) characterizing the spinel ferrites are clearly identified. The analysis of XRD patterns indicates that the investigated samples have formed the homogeneous single-phased cubic spinel structure belonging to

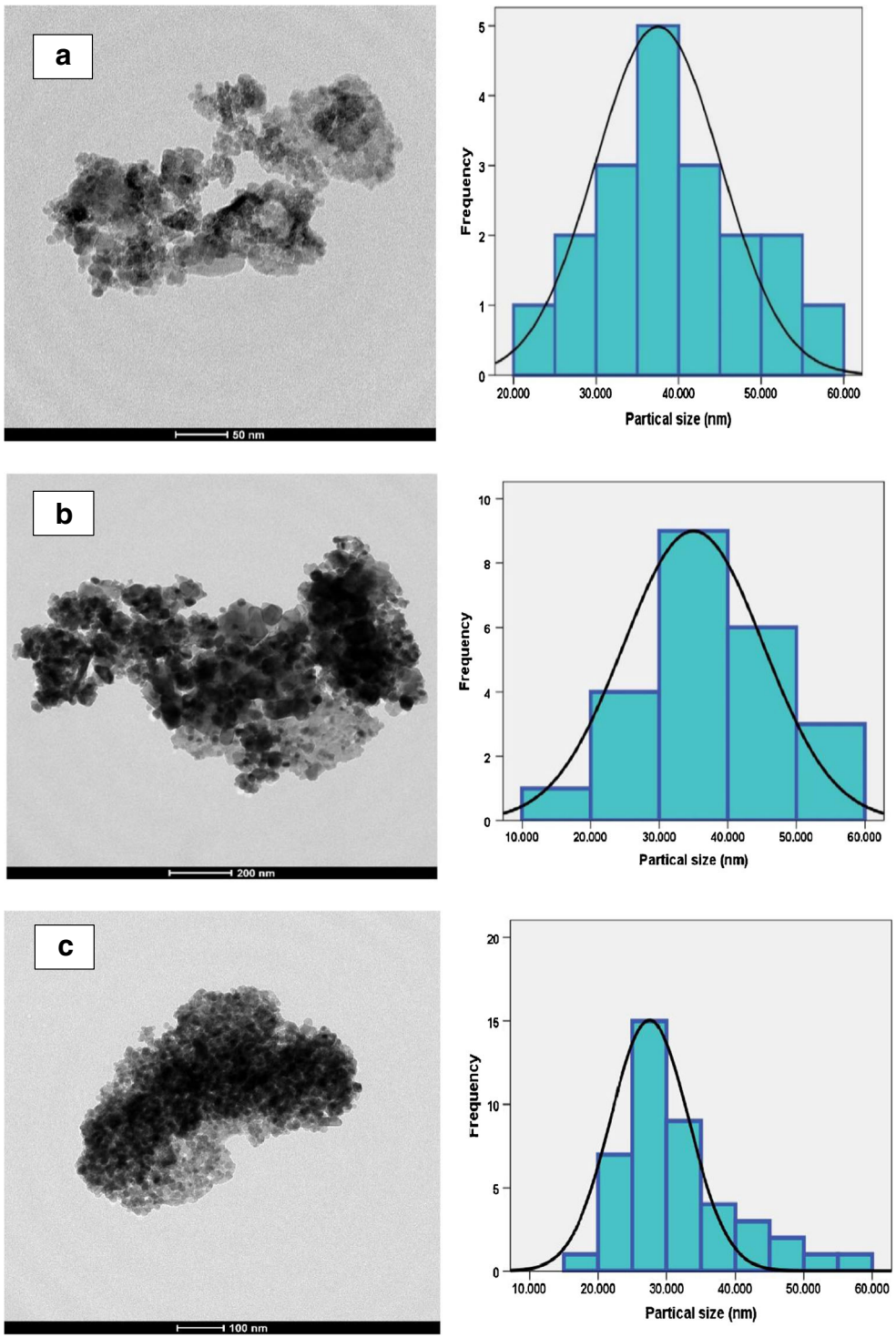

Fig. 2 **a**–**c**: HRTEM micrograph for $Mg_{1-x}Ni_xFe_2O_4$ for (**a**) x=0.0, (**b**) x=0.3 and (**c**) x=0.5

the space group Fd3m. The induced strain is calculated from the Williamson-Hall method [22] and is tabulated in Table 1. There is a small shifting of the diffraction peak towards higher 2θ as shown in Fig. 1. This means that the crystallite sizes are decreased due to the induced strain as shown in Table 1. The average crystallite size of the samples (D) is determined from the broadening of the respective high intensity (311) peak using the Debye Scherrer's formula [20]. The calculated data is discussed later.

The variation of the experimental lattice parameter (a_{exp}) with Ni^{2+} ion concentration (x) is tabulated in Table 1. From the table it is clear that the experimental lattice parameter decreases with increasing Ni^{2+} ions concentration in the spinel oxides $Mg_{1-x}Ni_xFe_2O_4$. This can be explained on the basis of the relative ionic radii of Ni^{2+}, Mg^{2+}, and Fe^{3+} ions present in the system. Since Ni^{2+} ions have smaller ionic radii (0.69 Å), than Mg^{2+} ions (0.72 Å) in the octahedral sites, a partial replacement of the Mg^{2+} ions by the Ni^{2+} ions causes shrinkage of unit cell dimensions, thereby decreasing the lattice parameter. The experimental lattice parameter decreases gradually with increasing x values satisfying Vegard's law [23]. The theoretical lattice parameter (a_{th}) can be calculated [24] by using the expected cation distribution of the system as shown later. The obtained data is given in the table. The small deviation between the theoretical lattice parameter and the experimental one indicates that the cation distribution is redistributed due to the preparation conditions.

High resolution transmission electron microscope (HRTEM) images and histograms of the $Mg_{1-x}Ni_xFe_2O_4$ are shown in Fig. 2a–c. The images show that the particles have a nearly homogeneous distribution. Micrographs for x=0.3, 0.5 show highly agglomerated states of nanoparticles due to their mutual magnetic interactions. It is evident from the HRTEM images that the aggregation of particles lies in the nanometric region as shown in Table 2. The particles are observed as uniform grains without any impurity confirming the crystalline structure of Mg-Ni nano-ferrites which are detected by the XRD studies.

Surface roughness of nano-crystalline ferrites is characterized using the AFM. Representative AFM micrographs of the investigated samples are presented in Fig. 3a–c and the estimated particle sizes are tabulated in Table 2. It is clear from the table that the pure nickel has the highest particle size. This is because nickel needs a high sintering temperature T = 800 °C to be prepared compared with other concentrations. The particle sizes estimated from HRTEM and AFM are somewhat greater than the crystallite size estimated from XRD. This is because the X-ray diffraction pattern gives the data for the crystalline region only and the contribution from the amorphous grain surface is not included. By analyzing HRTEM, AFM and XRD data one can have a nearly complete picture of the particles size, distribution and morphology.

The surface area, average pore size and pore volume of the investigated samples were determined and are reported in Table 2. The pore size distribution confines the shape selectivity and the effectiveness of the adsorbents ion-exchangers. The investigated samples possess extremely high surface areas and narrow pore size distributions depending on Ni ion concentration. The inset of Fig. 3a shows the variation of pore size versus pore volume. The higher peaks indicate the pore sizes that contribute the most to the overall porosity. AFM micrographs for x = 0.0, 0.3 (in the same figure) show the type of porosity reflected by the graph. The surface area of the samples decrease from 74.6 m^2/g to 21.4 m^2/g.

EDAX analysis of the investigated samples confirmed the stoichiometric ratio of a given system as shown in Fig. 4a–c.

The atomic percentage (at.%) and weight percentage (wt.%) of constituent elements (Ni, Mg, Fe and O) are calculated theoretically from the intermediate chemical composition $Mg_{1-x}Ni_xFe_2O_4$. The obtained data from EDAX elemental analysis are shown in the inset of Fig. 4a–c. The elemental analysis as obtained from EDAX is in close agreement with the starting materials used for the synthesis. The difference between the values of the atomic ratio as determined by EDAX and the expected value can be attributed to surface crystalline defects of the nano-particles.

Figure 5a shows hysteresis loops for $Mg_{1-x}Ni_xFe_2O_4$ ($0.0 \leq x \leq 1.0$). The area within the M-H loop represents a magnetic energy loss. This area for all the samples is small which is a specific feature for a soft ferrite. Parameters such

Table 2 Values of crystallite size from X-ray analysis and particle size from HRTEM, AFM microscopy, the BET surface area, pore volume, and average pore diameter for $Mg_{1-x}Ni_xFe_2O_4$ (x =0.0, 0.3, 0.5 and 1.0)

Ni content (x)	Crystallite size XRD (nm)	Particle size HRTEM (nm)	Particle size AFM (nm)	Surface area (m^2/g)	Average pore volume (CC/g)	Average pore diameter (nm)
0.0	27.60	37.50	37.50	74.60	0.11	2.24
0.3	26.00	35.00	30.00	21.80	0.06	2.23
0.5	24.60	27.50	32.50	57.50	0.12	0.24
1.0	40.20	–	45.00	21.40	0.06	0.23

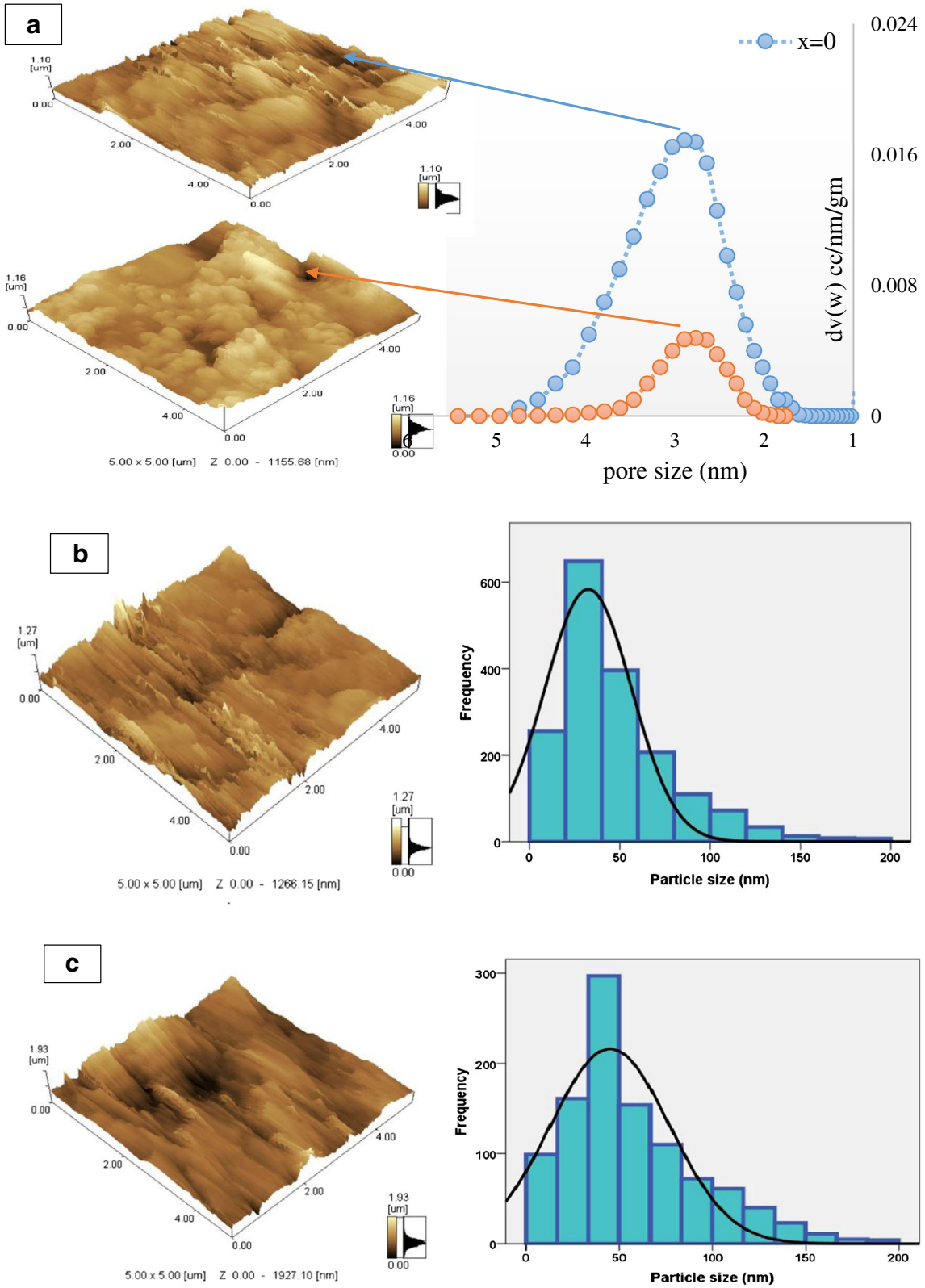

Fig. 3 **a**–**c**: Represent 3D atomic force microscopy for $Mg_{1-x}Ni_x$ Fe_2O_4 for (**a**) x=0.0 and x=0.3. (The insets represent the pore size distribution for the two samples), (**b**) x=0.5 and (**c**) x=1.0

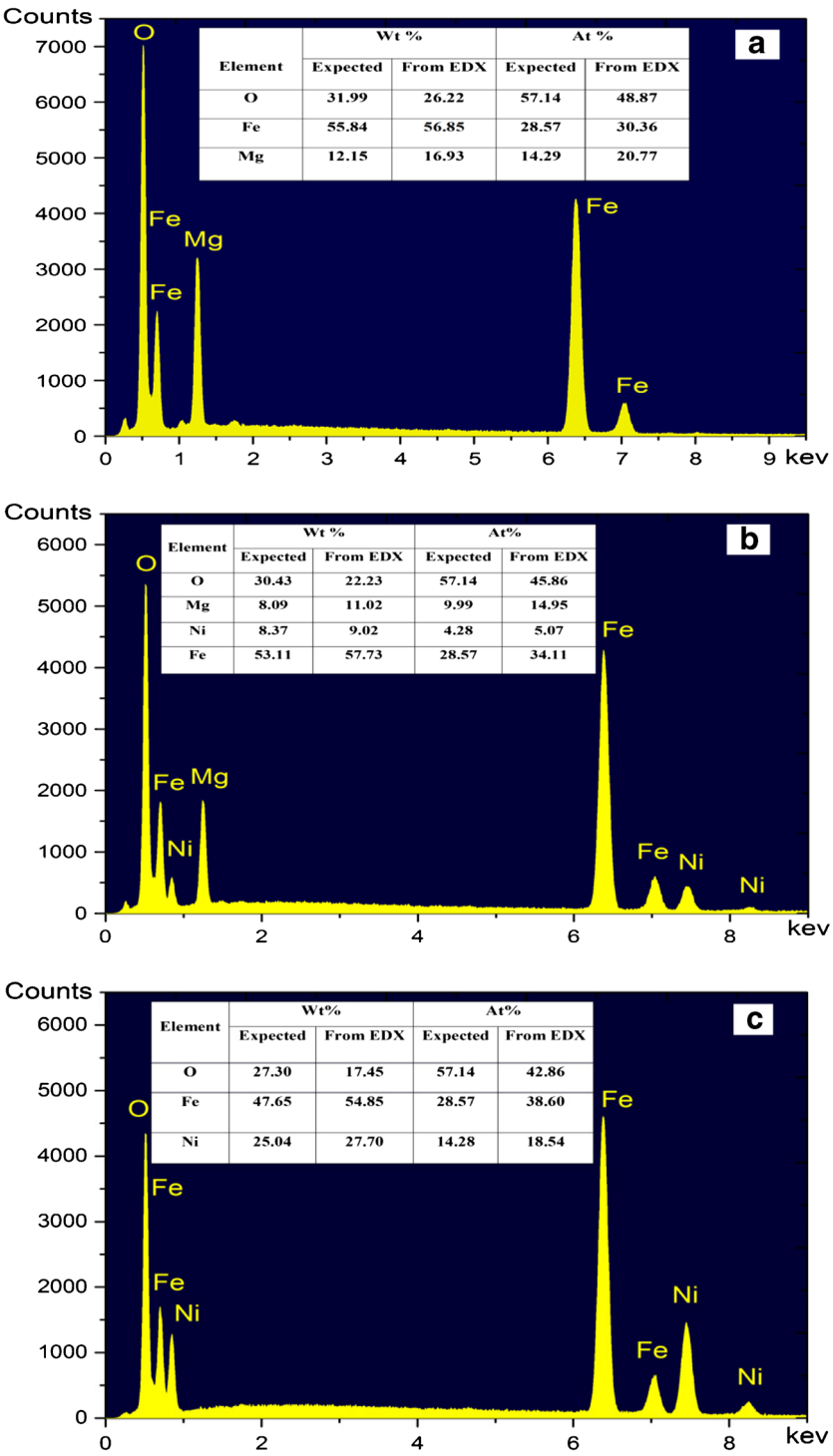

Fig. 4 **a–c**: EDAX images for samples $Mg_{1-x}Ni_x\ Fe_2O_4$ for (**a**) x=0.0, (**b**) x=0.3 and (c) x=0.5. The inset tables give quantitative estimation of elements obtained directly from the spectrum through its weight and atomic percentages

as saturation magnetization (M_s), remnant magnetization (M_r) and coercivity (H_c) are determined from the hysteresis loop for various Ni^{2+} ion concentrations and are tabulated in Table 3. The variation of M_s and M_r with Ni content can be explained on the basis of exchange interactions between ions at tetrahedral (A) and octahedral (B) sites [25]. Replacement of nonmagnetic Mg^{2+} ($0\mu B$) ions by magnetic Ni^{2+} ion ($2\mu B$) enhances the magnetization of the B site. Hence the overall effect of Ni-substitution is the gradual rising in M_s and M_r. The coercivity Hc of the investigated samples increases with increasing Ni^{2+} ion concentration. This can be attributed to the gain of anisotropy due to the migration of Mg^{2+} ions to the tetrahedral site. The Hc values vary from 56.4 Oe to 130 Oe. These

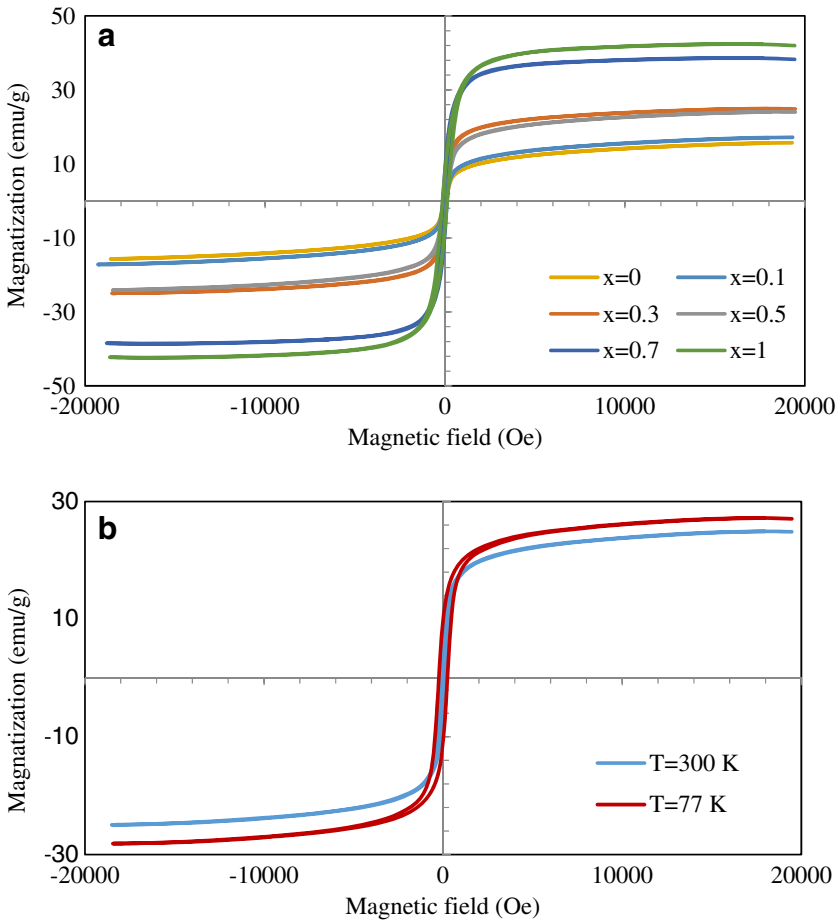

Fig. 5 **a–b**: Magnetic hysteresis loops for (**a**) $Mg_{1-x}Ni_x\ Fe_2O_4$ ($0.0 \leq x \leq 1.0$) at 300 K and (**b**) $Mg_{0.7}\ Ni_{0.3}\ Fe_2O_4$ at 300 K and 77 K

values make the investigated samples well suited for their use in recording media. The values in this range are required for such media in order to avoid the loss of data bits [26]. The variation in the value of the saturation magnetization with particle size may result from the cation redistribution.

The magnetic behavior is strongly influenced by surface roughness (obtained from AFM). The maximum saturation magnetization is obtained for $Mg_{0.3}Ni_{0.7}Fe_2O_4$ nano-ferrite with lower surface roughness of 0.73 compared to the other concentrations. The obtained squareness ratio (M_r/M_s) for Ni doped Mg samples is less than 0.5 as shown in Table 3. This means that the particles only interact by magnetostatic interactions. Also the small value of the squareness may be due to the presence of non-interacting single domain particles with cubic anisotropy in the investigated samples [27]. The M_s values are used to estimate magnetic moment per unit formula (n_B) in terms of the Bohr magneton (μB) using the formula [28]

$$n_B = \frac{Molecular\ weight\ x\ saturation\ magnetization}{5585} \quad (1)$$

Table 3 Values of Saturation magnetization, Remnant magnetization, Coercive field, Squarness, Energy loss, experimental and theoretical Magnetic moment (n_B) and Roughness for $Mg_{1-x}Ni_x\ Fe_2O_4$ ($0.0 \leq x \leq 1.0$) at 300 K and x=0.3 at 77K

Ni content (x)		M_s (emu/gm)	M_r (emu/gm)	H_c (Oe)	(M_r/M_s)	Energy loss (J/gm) $\times 10^{-4}$	n_B (exp)	n_B (theo)	Roughness (μm)
0.0		15.71	1.67	71.54	0.11	4.27	0.56	1.00	1.17
0.1		17.18	1.47	56.45	0.09	4.68	0.63	1.10	–
0.3	300K	24.95	5.22	101.13	0.21	9.96	0.94	1.30	0.73
	77 K	27.70	9.90	235.70	0.40	23.70	–	–	–
0.5		24.07	3.52	95.47	0.15	9.09	0.94	1.50	1.15
0.7		38.52	7.97	118.07	0.21	18.65	1.55	1.70	–
1.0		42.37	7.45	130.25	0.18	18.91	1.78	2.00	0.61

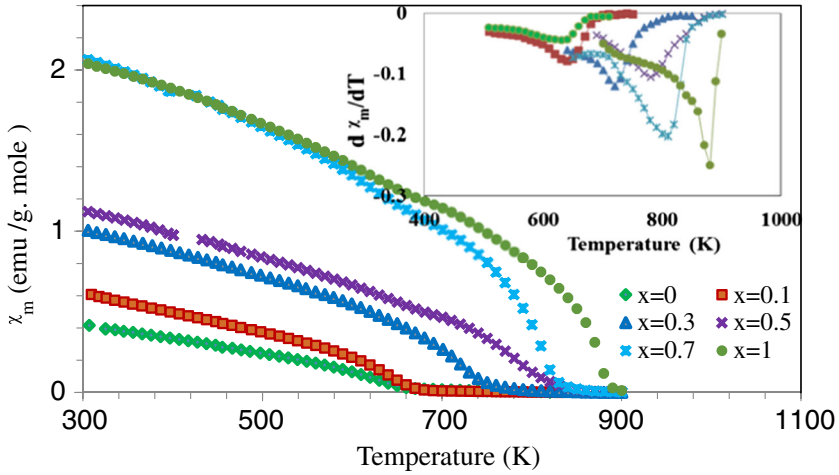

Fig. 6 Magnetic susceptibility versus temperature for $Mg_{1-x}Ni_xFe_2O_4$ ($0.0 \leq x \leq 1.0$). The inset shows the 1st derivative of magnetic susceptibility with temperature

The calculated n_B values are compared with the theoretical ones, $n_B = M_B - M_A$, where M_A and M_B are the cation distribution of sites A and B respectively. The magnetic moment per unit formula is calculated using both the magnetic moment of each cation, (5, 4, 2 and 0 for Fe^{3+}, Fe^{2+}, Ni^{2+} and Mg^{2+}, respectively), and the estimated cation distributions (listed in Table 1). The calculated data are tabulated in Table 3. The mismatching between the experimental and theoretical magnetic moment can be attributed to the surface and local spin canting effects of the present samples. The Yafet-Kittel [29] magnetic ordering of the local moments may further explain the small values of n_B.

Figure 5b shows the hysteresis loops at 77 K and 300 K for $Mg_{0.7}Ni_{0.3}Fe_2O_4$. The same behavior is obtained for both temperatures. However the saturation magnetization at 77 K is larger than that at 300 K. This is because at high temperature thermally induced randomness is high which decreases the magnetization. On the other hand, the random orientation of spins at high temperature causes the coercivity to be low as shown in Table 3.

The increase in H_c is more prominent at lower temperature, 77 K. It is well known that as the measurement temperature goes beyond the Curie temperature of magnetic materials, the materials become more and more anisotropic [30] that causes an enhancement in coercivity of the subjected materials. In the case of the investigated samples, the value of coercivity at 77 K is found to be twice as large as H_c at 300 K. This increase may be explained on the basis of domain structure, critical diameter, strains and shape anisotropy of the crystal [31]. As shown from the table at low temperature the squareness ratio is increased but is still lower than 0.5.

Figure 6 correlates the molar magnetic susceptibility with the absolute temperature at constant magnetic field intensity ($H = 5000$ Oe). From the figure it is clear that χ_M decreases steadily with increasing temperature then decreases rapidly to reach its minimum value at the Curie temperature T_c.

The material changes its ferromagnetic nature and becomes paramagnetic at T_c and the molar magnetic susceptibility of paramagnetic materials decreases with increasing temperature. This confirms the absence of any impurity in the investigated samples leading to the conclusion that a single spinel phase is formed as already predicted from the XRD analysis. The inset of Fig. 6 shows $\frac{d\chi_M}{dT}$ from which one can determine the Curie temperature of the investigated samples. The change of Curie temperature (T_c) with Ni^{2+} content is shown in Table 4. The obtained data obey the well-known Curie–Weiss law where χ varies linearly with temperature in the paramagnetic region. The values of the Curie constant (C) and the effective magnetic moment (μ_{eff}) are calculated from the reciprocal of magnetic susceptibility with absolute temperature [32]. The Curie-Weiss constant (θ) is calculated from the intercept of the straight line with the temperature axis. The experimental data is fitted linearly and the magnetic parameters are calculated and tabulated in Table 4.

Table 4 The Magnetic constants: Curie temperature (T_c),Curie constant (C), Weiss constant (θ) ,and Effective magnetic momment (μ_{eff}) for $Mg_{1-x}Ni_xFe_2O_4$($0.0 \leq x \leq 1.0$)

Ni content (x)	C (emu. K/gm. mole)	μ_{eff}(B. M)	θ (K)	T_c (K)
0.0	0.15	1.10	620	625
0.1	0.21	1.30	640	638
0.3	0.47	1.90	720	725
0.5	0.37	1.70	775	783
0.7	0.86	2.60	815	813
1.0	0.96	2.80	860	870

As shown from the Table T_c and μ_{eff} increase linearly with increasing Ni^{2+} content. This can be explained on the basis of the number of magnetic ions present in the two sub-lattices and their mutual interactions. As Mg^{2+} ions are gradually replaced by Ni^{2+} ions, the number of strong magnetic ions begins to increase at the octahedral site which increases the strength of B-B exchange interactions. Thus, more thermal energy is required to offset the spin alignment thereby increasing the Curie temperature in the investigated system. The increase in T_c with increasing concentration of Ni may be also explained by a modification of the A-B exchange interaction strength due to the change of Fe^{3+}distribution between A and B sites.

4 Conclusion

1. X-ray diffraction (XRD) studies confirm the formation of the cubic spinel structure without any impurity phase.
2. The crystallite sizes of the investigated nano-ferrites are in the range of 24.6-27.6 nm.
3. EDAX analysis of the investigated samples confirms the stoichiometric ratio of a given system.
4. The low temperature has a great effect on magnetic parameters of Mg-Ni samples.
5. The coercivity (H_c) values vary from 56.4 Oe to 130 Oe. These values make the investigated samples well suited for their use in recording media.
6. The physical properties of $Mg_{0.7}Ni_{0.3}Fe_2O_4$ demonstrate suitable crystalline size, high value of magnetization, low roughness and low porosity. Thus this guarantees hope for technological applications at or below room temperature.

References

1. Msomi JZ, Dlamini WB, Moyo T, Ezekiel P (2015) Investigation of Phase formation of (Zn, Mg)0.5CoFe2O4. Magn Magn Mater 373:68–73
2. Masina P, Moyo T, Abdallah HMI (2015) Structural and magnetic properties of MnxCo1–xFe2O4 ferrite nanoparticles. Magn Magn Mater 381:41–49
3. Bhukal S, Sharma R, Mor S, Singhal S (2015) Mg–Co–Zn magnetic nanoferrites: Characterization and their use for remediation of textile wastewater. Superlattices Microstruct 77:134–151
4. Wahba AM, Mohamed MB (2014) Structural, magnetic, and dielectric properties of nanocrystalline Cr-Substituted Co0.8Ni0.2Fe2O4 Ferrite. Cerm Int 40:6127–6135
5. Kumar G, Shah J, Kotnala RK, Singh VP, Sarveena G Garg, Shirsath SE, Batoo KM, Singh M (2015) Superparamagnetic behaviour and evidence of weakening in super-exchange interactions with the substitution of Gd3+ ions in the Mg-Mn nanoferrite matrix. Mater Res Bull 63:216–225
6. Moura EM, Garcia MAS, Gonçalves RV, Kiyohara PK, Jardimc RF, Rossi LM (2015) Gold nanoparticles supported on magnesium ferrite and magnesium oxide for the selective oxidation of benzyl alcohol. RSC Adv 5:15035–15041
7. Goldman A (2006) Modern ferrite technology, 2nd edn. Springer, Pittsburgh, pp 51–61
8. Godbole RV, Rao P, Alegaonkar PS, Bhagwat S (2015) Influence of fuel to oxidizer ratio on LPG sensing performance of MgFe2O4 nanoparticles. Mater Chem Phys 161:135–141
9. Han X, Tian P, Pang H, Song Q, Ning G, Yu Y, Fang H (2014) Facile synthesis of magnetic hierarchical MgO–MgFe2O4composites and their adsorption performance towards Congo red. RSC Adv 4:28119–28125
10. Loganathan A, Kumar (2016) Effects on structural, optical, and magnetic properties of pure and Sr-substituted MgFe2O4 nanoparticles at different calcination temperatures. Appl Nanosci 6(5):629–639. https://doi.org/10.1007/s13204-015-0480-0
11. Bamzai KK, Kour G, Kaur B, Kulkarni SD (2013) Effect of cation distribution on structural and magnetic properties of Dy substituted magnesium ferrite. Magn Magn Mater 327:159–166
12. Gaffoor A, Ravinder D (2014) Characterization of magnesium substituted nickel nano ferrites synthesized by citrate-gel auto combustion method. Eng Res Appl 4:60–66
13. Hoque SM, Hakim1 MA, Mamun A, Akhter S, Hasan MT, Paul DP, Chattopadhayay K (2011) Preparation and characterization of nanosized magnesium ferrite. Mater Sci Appl 2:1564–1571
14. Tholkappiyan R, Vishista K (2015) Combustion synthesis of Mg–Er ferrite nanoparticles: Cation distribution and structural, optical, and magnetic properties. Mater Sci Semicond Process 40:631–642
15. Franco A Jr, Silva MS (2011) High temperature magnetic properties of magnesium ferrite nanoparticles. J Appl Phys 109: 075055eB513
16. Albuquerque AS, Ardisson JD, Macedo WAAA, Alves MCM (2000) Nanosized powders of NiZn ferrite: Synthesis, structure, and magnetism. J Appl Phys 87:4352–4357
17. Ateia EE, Mohamed AT (2017) Improvement of the Magnetic Properties of Magnesium Nanoferrites Via Co^{2+}/Ca^{2+} Doping. J Supercond Nov Magn 30:627–633
18. Ateia EE, Mohamed AT (2017) Correlation between the physical properties and the novel applications of $Mg_{0.7}Cu_{0.3}Fe_2O_4$ nanoferrites. J Mater Sci: Mater Electron 28:10035–10041
19. Mazen SA, Mansour SF, Zaki HM (2003) Some physical and magnetic properties of Mg-Zn ferrite. Cryst Res Technol 38(6):471–478
20. Amer MA, Meaz T, Yehia M, Attalah SS, Fakhry F (2015) Characterization, structural and magnetic properties of the as-prepared Mg-substituted Cu-nanoferrites. Alloys Compd 633:448–455
21. Schüth F, Sing KSW, Weitkamp J (2002) Handbook of porous solids, vol 1. Wiley-VCH, Weinheim
22. Prabhu1 YT, Rao KV, Kumar VSS, Kumari BS (2014) X-Ray analysis by Williamson-Hall and size-strain plot methods of ZnO nanoparticles with fuel variation. Nano Sci Eng 4:21–28
23. Kingery WD, Bowen HK, Uhlmann DR (1976) Introduction to ceramics, 2nd edn. Wiley, New York, p 131
24. Wahba AM, Mohamed MB (2014) Structural, magnetic, and dielectric properties of nanocrystalline Cr-substituted $Co_{0.8}Ni_{0.2}Fe_2O_4$ ferrite. Ceram Int 40:6127–6135
25. Deraz NM (2012) Effects of magnesia addition on structural, morphological and magnetic properties of nanocrystalline nickel ferrite system. Ceram Int 38:511–516
26. Saranu S, Selve S, Kaiser U, Han L, Wiedwald U, Ziemann P, Leiderer UHP (2011) Effect of large mechanical stress on the

magnetic properties of embedded Fe nanoparticles. Nanotechnol 2:268–275
27. Obaidat IM, Issa B, Haik Y (2015) Magnetic properties of magnetic nanoparticles for efficient hyperthermia. Nanomater Nanotechno 5(1):63–89
28. Moradmard H, Shayesteh SF, Tohidi P, Abbas Z, Khaleghi M (2015) Structural, magnetic and dielectric properties of magnesium doped nickel ferrite Nanoparticles. Alloys Compd. https://doi.org/10.1016/j.jallcom.(2015).07.269
29. Nikam DS, Jadhav SV, Khot VM, Bohara RA, Hong CK, Mali SS, Pawar SH (2015) Cation distribution, structural, morphological and magnetic properties of $Co_{1-x}Zn_xFe_2O_4$ ($x = 0-1$) nanoparticles. RSC Adv 5(3):2338
30. Alvarez G, Montiel H, Barron JF, Gutierrez MP, Zamorano R (2010) Yafet–Kittel-type magnetic ordering in $Ni_{0.35}Zn_{0.65}Fe_2O_4$ferrite detected by magnetosensitive microwave absorption measurements. Magn Magn Mater 322:348
31. Nawale AB, Kanhe NS, Patil KR, Bhoraskar SV, Mathe VL, Das AK (2011) Magnetic properties of thermal plasma synthesized nanocrystalline nickel ferrite ($NiFe_2O_4$). Alloys Compd 509(12):4404–4413
32. Ateia EE, Abdelatif G, Ahmed MA, AbdAlla Mahmoud M (2015) Effect of different Gd^{3+} ion content on the electric and magnetic properties of lithium antimony ferrite. Inorg Organomet Polym Mater 25:81–90